

Atomic hydrogen in star-forming galaxies at intermediate redshifts

APURBA BERA,¹ NISSIM KANEKAR,^{1,*} JAYARAM N. CHENGALUR,¹ AND JASJEET S. BAGLA²

¹*National Centre for Radio Astrophysics, Tata Institute of Fundamental Research, Ganeshkhind, Pune - 411007, India*

²*Indian Institute of Science Education and Research Mohali, Knowledge City, Sector 81, Sahibzada Ajit Singh Nagar, Punjab 140306, India*

ABSTRACT

We have used the upgraded Giant Metrewave Radio Telescope to carry out a deep (117 on-source hours) L-band observation of the Extended Groth Strip, to measure the average neutral hydrogen (HI) mass and median star formation rate (SFR) of star-forming galaxies, as well as the cosmic HI mass density, at $0.2 < z < 0.4$. This was done by stacking the HI 21 cm emission and the rest-frame 1.4 GHz radio continuum from 445 blue star-forming galaxies with $M_B \leq -17$ at $z_{\text{mean}} \approx 0.34$. The stacked HI 21 cm emission signal is detected at $\approx 7\sigma$ significance, implying an average HI mass of $\langle M_{\text{HI}} \rangle = (4.93 \pm 0.70) \times 10^9 M_{\odot}$. We also stacked the rest-frame 1.4 GHz radio continuum emission of the same galaxies, to obtain a median SFR of $(0.54 \pm 0.06) M_{\odot} \text{ yr}^{-1}$; this implies an average atomic gas depletion time scale of $\langle \Delta t_{\text{HI}} \rangle \approx 9$ Gyr, consistent with values in star-forming galaxies in the local Universe. This indicates that the star-formation efficiency does not change significantly over the redshift range $0 - 0.4$. We used the detection of the stacked HI 21 cm emission signal to infer the normalized cosmic HI mass density ($\rho_{\text{HI}}/\rho_{\text{c},0}$) in star-forming galaxies at $z \approx 0.34$. Assuming the local relation between HI mass and absolute B-magnitude, we obtain $\rho_{\text{HI}}/\rho_{\text{c},0} = (4.81 \pm 0.75) \times 10^{-4}$, implying no significant evolution in $\rho_{\text{HI}}/\rho_{\text{c},0}$ from $z \approx 0.4$ to the present epoch.

Keywords: galaxies: evolution — galaxies: star formation — radio lines: galaxies — radio continuum: galaxies

1. INTRODUCTION

Understanding galaxy evolution requires us to understand evolution in the two main baryonic constituents of galaxies, the stars and the gas. Over the last two decades, much progress has been made in understanding the evolution of the stellar properties of galaxies (e.g. the star formation rate (SFR), the main sequence, etc; Hopkins & Beacom 2006; Noeske et al. 2007), via optical and near-infrared studies of the so-called “deep fields”. Our understanding of molecular gas in high- z galaxies has also improved, via blind and targeted CO studies (e.g. Tacconi et al. 2018; Pavese et al. 2018; Decarli et al. 2019). In contrast, little is known about atomic gas, primarily neutral hydrogen (HI), in high- z galaxies, although this is the primary fuel reservoir for star formation. Understanding the redshift evolution of the HI content of star-forming galaxies is essential to obtain a complete picture of galaxy evolution.

In the local Universe, HI 21 cm emission surveys have yielded the HI masses of thousands of galaxies (e.g. Zwaan et al. 2005; Jones et al. 2018), providing accurate measurements of the HI mass function and the cosmic HI mass density. Unfortunately, it is difficult to detect the weak HI 21 cm line from galaxies at $z \gtrsim 0.2$ with current telescopes (e.g. Jaffé et al. 2013; Catinella & Cortese 2015), with only one galaxy detected at $z \gtrsim 0.25$, at $z \approx 0.376$ in the Very Large Array CHILES survey of the COSMOS field (Fernández et al. 2016).

While detecting individual galaxies in HI 21 cm emission at $z \gtrsim 0.3$ will require very deep integrations in the foreseeable future, one can measure the average HI content of samples of galaxies within the primary beam of a radio interferometer, by “stacking” their HI 21 cm emission signals (e.g. Chengalur et al. 2001). Of course, such stacking requires large galaxy samples with accurate redshifts, usually from optical spectroscopy. This requirement has meant that, despite multiple studies, there are still no statistically-significant detections of the stacked HI 21 cm emission signal at $z \gtrsim 0.2$ (e.g. Lah et al. 2007; Kanekar et al. 2016; Rhee et al. 2018).

The paucity of information on the HI content of galaxies at even relatively low redshifts, $z \gtrsim 0.25$, has motivated us to

Corresponding author: Apurba Bera
apurba@ncra.tifr.res.in

* Swarnajayanti Fellow

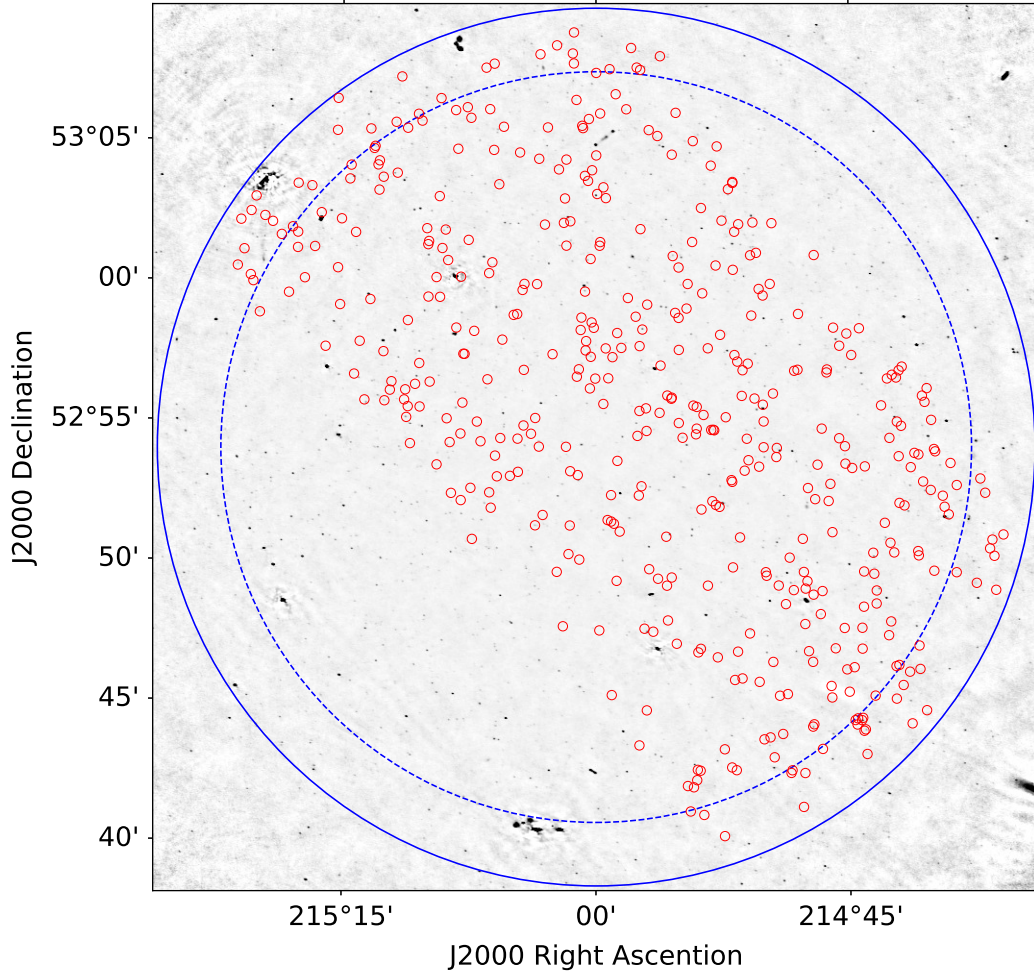


Figure 1. The uGMRT 1.2 GHz image of the EGS. The solid and dashed blue circles indicate the FWHM of the uGMRT primary beam at 1014 MHz ($z = 0.4$) and 1183 MHz ($z = 0.2$), respectively. The red circles indicate the locations of the 445 galaxies of our sample.

begin an HI 21 cm “deep field” with the upgraded Giant Metrewave Radio Telescope (uGMRT). We chose the Extended Groth Strip (EGS) as the target field, due to the outstanding ancillary data in the EGS over a wide range of wavelengths, as well as the excellent spectroscopic coverage in this field from the DEEP2 and DEEP3 surveys (Newman et al. 2013; Cooper et al. 2012). In this *Letter*, we present results from the first part of this uGMRT HI 21 cm emission survey¹.

2. OBSERVATIONS & DATA ANALYSIS

We used the uGMRT L-band receivers to carry out a deep integration on the EGS between March 2017 and April 2018 (proposals 31.038 and 34.083). The total integration time was ≈ 175 hours, with an on-source time of ≈ 117 hours. The pointing centre was chosen to be RA=14h20m00.0s, Decn.=+52°54′00.0″, close to the centre of the region with the richest multi-wavelength coverage. The GMRT Wide-

band Backend was used as the correlator, with a bandwidth of 400 MHz, sub-divided into 8192 channels, and two polarizations. The 400 MHz band covers the frequency range 970 – 1370 MHz, corresponding to $z \approx 0.037 - 0.46$, with a velocity resolution of $\approx 10 - 15 \text{ km s}^{-1}$ across the band.

The initial analysis, including data editing, and gain and bandpass calibration was carried out using “classic” AIPS, following standard procedures. After the initial calibration, the 400 MHz dataset was split into four 100-MHz sub-bands, and a standard self-calibration procedure (e.g. Kanekar et al. 2016) was then run independently in AIPS on each sub-band. The self-calibrated data of the four sub-bands were then stitched together, and the combined visibilities imaged in CASA, using TCLEAN. An area of $\approx 1^\circ \times 1^\circ$ was imaged, out to the first null of the uGMRT primary beam. A single final amplitude-and-phase self-calibration was then carried out to bring the different sub-bands onto the same flux density scale, and a final continuum image then made from the self-calibrated data, using TCLEAN, with Briggs weighting (robust=0.5). This image, shown in Fig. 1, has a resolution

¹ We use a Lambda Cold Dark Matter “737” cosmology, with $\Omega_m = 0.3$, $\Omega_\Lambda = 0.7$, and $H_0 = 70 \text{ km s}^{-1} \text{ Mpc}^{-1}$, throughout this manuscript

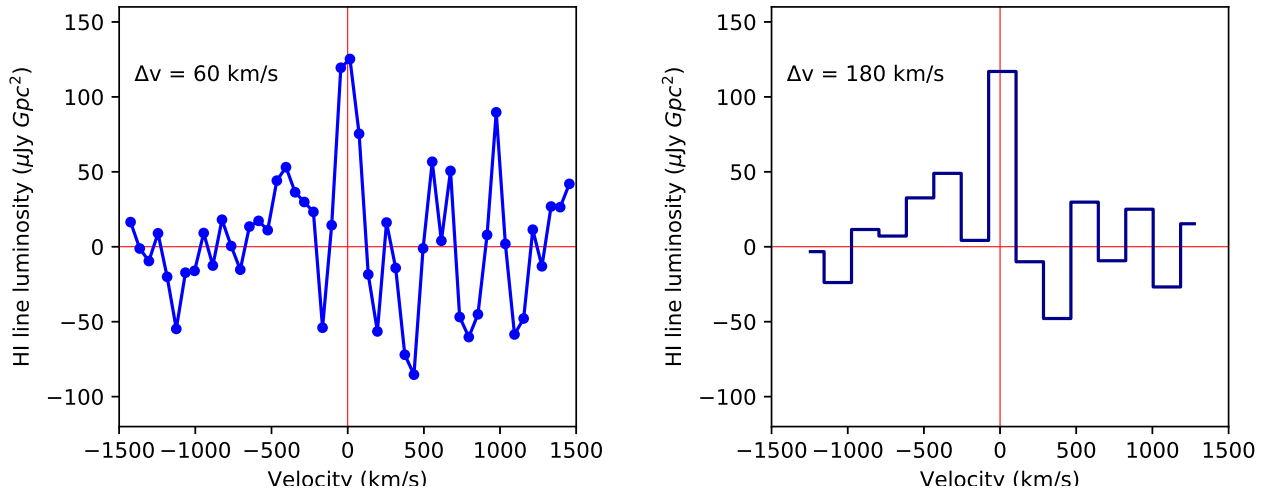


Figure 2. The stacked HI 21 cm emission spectrum of the 445 galaxies of our sample, at velocity resolutions of 60 km s^{-1} (left panel) and 180 km s^{-1} (right panel).

of $\approx 3.5'' \times 2.7''$ and a root-mean-square (RMS) noise of $\approx 2.3 \mu\text{Jy/Bm}$ near the image centre.

The gain solutions obtained from the self-calibration procedure were then applied to the spectral visibilities, and the continuum image subtracted out, before a final round of RFI excision was carried out on the residual data. The residual multi-channel visibilities were then shifted to the barycentric frame and imaged in CASA, using natural weighting. This spectral cube was corrected for the (frequency-dependent) shape of the uGMRT primary beam. Small sub-cubes were extracted at the location of each target galaxy, shifted to velocity, in the rest frame of the galaxy, and smoothed to, and re-sampled at, a velocity resolution of 60 km s^{-1} .

3. STACKING THE HI 21 cm EMISSION AND THE RADIO CONTINUUM

To obtain a clean interpretation of the HI 21 cm stacking results, it is important to use a uniformly-selected sample of galaxies, with accurate redshifts (redshift errors $\lesssim 100 \text{ km s}^{-1}$). For the EGS, the DEEP2 and DEEP3 surveys have a redshift accuracy of $\approx 30 \text{ km s}^{-1}$ (Newman et al. 2013), sufficient for HI 21 cm stacking. We restricted our target sample to “blue” star-forming galaxies, using the colour division of Coil et al. (2008) between red and blue galaxies, $[(U - B) = -0.032 \times (M_B + 21.62) + 1.035]$. We also used a uniform absolute B-magnitude limit to select our targets, with $M_B \leq -17$; with the DEEP2 and DEEP3 spectroscopic criteria, this yields a near-complete, absolute-magnitude-limited sample of galaxies at $0.2 < z < 0.4$. Finally, the galaxies were selected to lie within the full-width-at-half-maximum (FWHM) of the uGMRT primary beam at the frequency of the redshifted HI 21 cm line, to have redshift quality code > 3 (i.e. reliable redshifts; Newman et al. 2013), and to not be classified as active galactic nuclei in either the DEEP2/DEEP3 catalogs (based on the best-fit tem-

plate to the optical spectral energy distribution Cooper et al. 2012; Newman et al. 2013) or detected in our radio continuum image, with a 1.4 GHz luminosity $\geq 2 \times 10^{23} \text{ W Hz}^{-1}$ (e.g. Condon et al. 2002).

We do not *a priori* know the optimal spatial resolution at which to extract the spectrum for each galaxy. Using too high a resolution would resolve out some of the HI 21 cm emission, thus reducing the signal-to-noise ratio (S/N). Conversely, using too coarse a resolution would imply that only some of the interferometric baselines (the shorter ones) are being used to extract the spectrum, again lowering the S/N. We hence extracted spectra at a range of spatial resolutions, 20 – 100 kpc at the redshift of each galaxy, and stacked the spectra at each resolution, to determine the optimal spatial resolution. At each resolution, an error spectrum was also extracted for each galaxy, by measuring the RMS noise per channel in the sub-cube of the galaxy, from an annular region that excludes the galaxy itself. A second-order baseline was then fitted to each spectrum, using the velocity range $\pm 1500 \text{ km s}^{-1}$ around the galaxy redshift, and subtracted out.

Before stacking, we used the Kolmogorov-Smirnov and Anderson-Darling tests to test the spectra for Gaussianity, excluding spectra with p-values < 0.002 in either test. Our final sample contains 445 blue star-forming galaxies with $M_B \leq -17$, at $0.2 < z < 0.4$, and with an average redshift of $\langle z \rangle = 0.34$.

The stacking was carried out in units of HI 21 cm line luminosity (rather than flux density), to account for the spread in the luminosity distances of the target galaxies. While the uGMRT sensitivity is approximately constant (within $\approx 10\%$) across the observing band, the RMS noise on the flux density spectra varies due to both the galaxy locations in the primary beam and frequency-dependent data flagging. In addition, the RMS noise in the luminosity density spec-

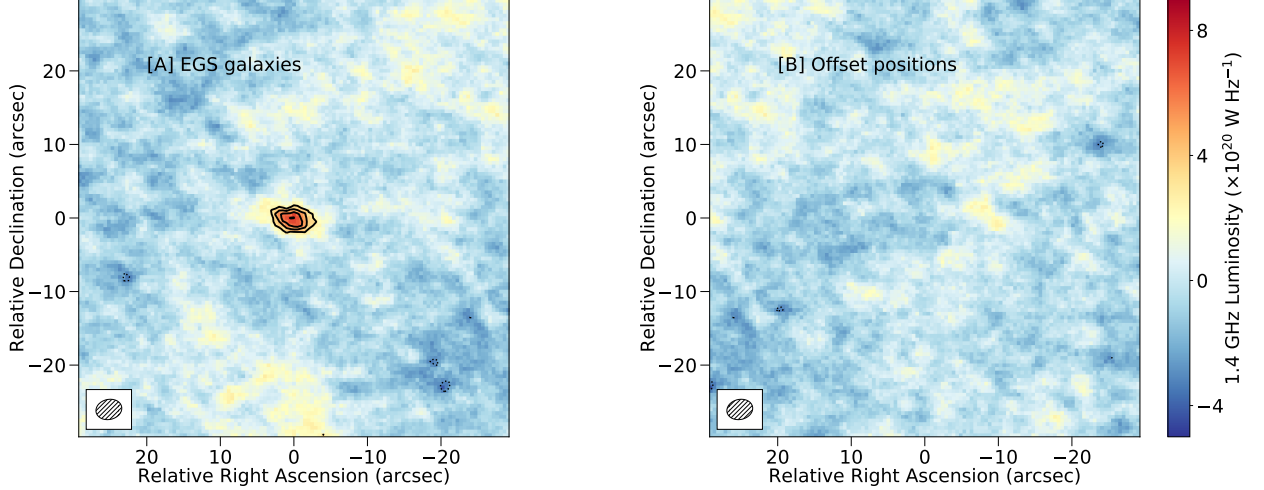


Figure 3. The stacked 1.4 GHz luminosity image (in units of $10^{20} \text{ W Hz}^{-1}$) from [A] (left panel) the 445 galaxies of our sample, and [B] (right panel) offset locations $50''$ away from the sample galaxies. The synthesized beam is shown as an ellipse in the bottom left.

tra increases with increasing redshift. The optimal approach of weighting by the inverse of the variance of the luminosity density spectra would imply significantly lower weights for the higher-redshift galaxies, i.e. a bias towards lower redshifts. We hence chose to weight each spectrum by the inverse of its variance in *flux density*, so that the effective redshift of the stacked spectrum remains the average redshift of the sample, $\langle z \rangle = 0.34$.

Our final stacked HI 21 cm spectrum, at a resolution of 40 kpc, is shown in Fig. 2. The spectrum shows a clear detection of HI 21 cm emission, with an integrated luminosity density of $L_{\text{HI}} = (2.10 \pm 0.30) \times 10^4 \text{ Jy Mpc}^2 \text{ km s}^{-1}$. The signal was also detected in the stacks at resolutions of 20 kpc and 30 kpc, but with a lower integrated luminosity density, indicating that the total HI 21 cm emission has not been recovered. Using a spatial resolution coarser than 40 kpc does not significantly change the integrated luminosity density, but lowers the S/N due to an increased RMS noise.

We also stacked the radio continuum images of our 445 galaxies, to measure their average SFR from the 1.4 GHz radio luminosity (e.g. Yun et al. 2001). We followed the procedure of Bera et al. (2018), using “median stacking” to stack the 1.4 GHz radio luminosity images of the sample. A radio spectral index of $\alpha = -0.8$ (with flux density $S_\nu \propto \nu^\alpha$) was assumed, to shift each galaxy’s image from the observing frequency of 1.2 GHz to a rest-frame frequency of 1.4 GHz.

Figure 3[A] shows the stacked 1.4 GHz continuum image of the 445 galaxies. A marginally resolved source is clearly detected, with a 1.4 GHz luminosity of $L_{1.4 \text{ GHz}} = (1.45 \pm 0.18) \times 10^{21} \text{ W Hz}^{-1}$. No emission was seen in a stack of positions offset by $50''$ from the sample galaxies, to test for possible systematic effects (see figure 3[B]; e.g. Bera et al. 2018).

4. RESULTS & DISCUSSION

4.1. The atomic gas mass and gas fraction

For optically-thin HI 21 cm emission, the HI mass of a galaxy is related to its velocity-integrated HI 21 cm line luminosity density by the relation

$$M_{\text{HI}} = 2.343 \times 10^5 \times \int L_{\text{HI}} dv, \quad (1)$$

where M_{HI} is in units of M_\odot and L_{HI} in $\text{Jy Mpc}^2 \text{ km s}^{-1}$. Our measured stacked HI 21 cm line luminosity density of $L_{\text{HI}} = (2.10 \pm 0.30) \times 10^4 \text{ Jy Mpc}^2 \text{ km s}^{-1}$ then yields an average HI mass of $\langle M_{\text{HI}} \rangle = (4.93 \pm 0.70) \times 10^9 M_\odot$, for the galaxies of the sample. The line FWHM is $\approx 200 \text{ km s}^{-1}$.

In the local Universe, the HI mass of a galaxy is correlated with its HI diameter, D_{HI} (e.g. Wang et al. 2016). If the local $D_{\text{HI}} - M_{\text{HI}}$ relation applies to galaxies at $z \approx 0.34$, our average HI mass of $\approx 5 \times 10^9 M_\odot$ implies an average diameter of $\approx 40 \text{ kpc}$. This is consistent with our finding that a spatial resolution of 40 kpc recovers all the HI 21 cm emission.

To estimate the effect of source confusion on the measured average HI mass, we identified galaxies in our sample with “close companion(s)”, defined as a neighbour separated by $\leq 40 \text{ kpc}$ and $\leq 300 \text{ km s}^{-1}$ in the DEEP2/DEEP3 catalogues. Only $\lesssim 10\%$ of the galaxies of our sample have such “close companion(s)”; excluding these from the stack does not significantly change the average HI mass. Source confusion thus has little effect on our measurement.

The average stellar mass of the galaxies of our sample is $\langle M_* \rangle = 4.1 \times 10^9 M_\odot$ (Mostek et al. 2012; Stefanon et al. 2017), implying a ratio of average HI mass to average stellar mass, $\langle M_{\text{HI}} \rangle / \langle M_* \rangle, \approx 1.2$. This is somewhat larger than values of M_{HI} / M_* in blue star-forming galaxies in the local Universe: for example, applying our stellar mass func-

tion to blue galaxies in the xGASS sample (with $\text{NUV-r} \leq 4$; Catinella et al. 2018) yields $M_{\text{HI}}/M_* \approx 0.5$ (although we note that the xGASS sample has $M_* \geq 10^9 M_\odot$, somewhat larger than the stellar mass of our sample).

4.2. The atomic gas depletion timescale

The atomic gas depletion timescale, $\delta t_{\text{HI}} = M_{\text{HI}}/\text{SFR}$, is the time taken by a galaxy to consume its HI reservoir at its current SFR, and is a measure of its star-formation efficiency. A short HI depletion time scale suggests that star formation is likely to soon be quenched, in the absence of gas inflow. In the local Universe, studies of stellar-mass-selected samples of star-forming galaxies (with, typically, $M_* \gtrsim 10^9 M_\odot$) have obtained $\Delta t_{\text{HI}} \approx 3 - 10$ Gyr, with little evidence for dependence on galaxy properties like stellar mass, galaxy colour, etc (e.g. Schiminovich et al. 2010; Wong et al. 2016; Saintonge et al. 2017; Catinella et al. 2018). However, stacking the HI 21 cm emission and the radio continuum of star-forming galaxies at $z \approx 1.3$ (with $M_B \lesssim -21$) yielded a far lower average HI depletion time, $\langle \Delta t_{\text{HI}} \rangle < 0.87$ Gyr (Kanekar et al. 2016; Bera et al. 2018). This suggests evolution in the HI depletion time for star-forming galaxies from $z \approx 1.3$ to $z \approx 0$.

Our stack of the 1.4 GHz radio continuum emission of 445 blue star-forming galaxies yielded a median 1.4 GHz radio luminosity of $L_{1.4 \text{ GHz}} = (1.45 \pm 0.18) \times 10^{21} \text{ W Hz}^{-1}$. Using the relation $\text{SFR} = 3.7 \times 10^{-22} \text{ W Hz}^{-1}$ (assuming a Chabrier initial mass function; Yun et al. 2001) gives a median SFR of $(0.54 \pm 0.06) M_\odot \text{ yr}^{-1}$. Combining this with the average HI mass yields $\langle \Delta t_{\text{HI}} \rangle \approx 9$ Gyr, consistent with the values of Δt_{HI} in the local Universe, but far lower than that at $z \approx 1.3$. This suggests either evolution in the star-formation efficiency of galaxies between $z \approx 1.3$ and $z \approx 0.34$, soon after the epoch of galaxy assembly, or a much higher efficiency in brighter galaxies at $z \approx 1.3$.

4.3. The cosmic HI density

Our estimate of the average HI mass, $\langle M_{\text{HI}} \rangle = (4.93 \pm 0.70) \times 10^9 M_\odot$, of an absolute-magnitude-limited sample of galaxies can be used to infer the cosmic mass density of HI in galaxies, $\rho_{\text{HI}}/\rho_{c,0}$, at $z \approx 0.34$, where $\rho_{c,0}$ is the comoving critical density at $z = 0$. To estimate $\rho_{\text{HI}}/\rho_{c,0}$ in galaxies with $M_B \leq -17$, we simply integrate over the B-band luminosity function at $z \approx 0.3$ for $M_B \leq -17$, and multiply by $\langle M_{\text{HI}} \rangle$. The B-band luminosity function at $z \approx 0.3$ is (Willmer et al. 2006)

$$\phi(L_B) = \left(\frac{\phi_*}{L_{B*}} \right) \left(\frac{L_B}{L_{B*}} \right)^\alpha e^{-L_B/L_{B*}}, \quad (2)$$

where $\phi_* = (32 \pm 2) \times 10^{-4} \text{ Mpc}^{-3}$, $L_{B*} = (1.77 \pm 0.09) \times 10^9 L_{B\odot}$ and $\alpha = -1.30$. Integrating over this luminosity function for $M_B \leq -17$ yields a comoving galaxy number

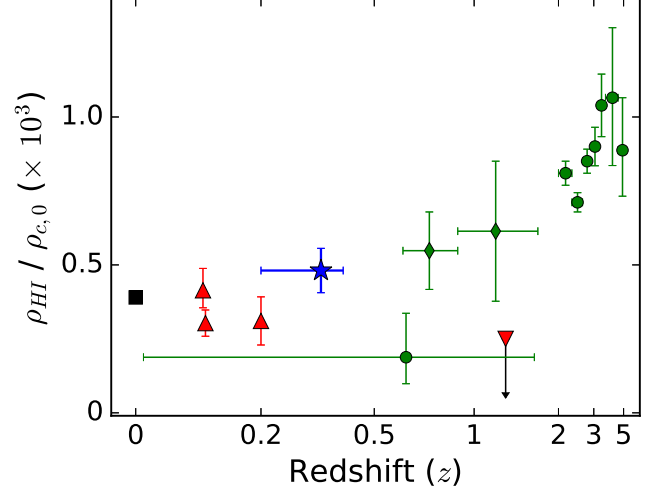


Figure 4. The evolution of $\rho_{\text{HI}}/\rho_{c,0}$ with redshift, with all values in a Λ CDM cosmology (Neeleman et al. 2016). The black square is from blind HI 21 cm emission surveys in the local Universe (Jones et al. 2018), the red triangles from earlier low- z HI 21 cm stacking experiments (with $\geq 3\sigma$ significance Rhee et al. 2013; Delhaize et al. 2013), the green circles from DLA studies (Noterdaeme et al. 2012; Crighton et al. 2015; Neeleman et al. 2016), and the green diamonds from MgII absorption samples (Rao et al. 2017). The inverted red triangle shows the 3σ upper limit on $\rho_{\text{HI}}/\rho_{c,0}$ in star-forming galaxies with $M_B \lesssim -21$ at $z \approx 1.3$ (Kanekar et al. 2016). The blue star shows the present measurement, at $z \approx 0.34$.

density of 0.013 Mpc^{-3} . This yields $\rho_{\text{HI}} = (6.41 \pm 0.91) \times 10^7 M_\odot \text{ Mpc}^{-3}$, and $\rho_{\text{HI}}/\rho_{c,0} = (4.75 \pm 0.67) \times 10^{-4}$ for galaxies with $M_B \leq -17$ at $0.2 < z < 0.4$. We emphasize that this estimate of $\rho_{\text{HI}}/\rho_{c,0}$ does *not* include contributions from galaxies fainter than $M_B = -17$.

The total $\rho_{\text{HI}}/\rho_{c,0}$ in blue galaxies at $z \approx 0.3$ may be estimated by combining the B-band luminosity function at $z \approx 0.3$ with the relation between M_{HI} and M_B (e.g. Dénes et al. 2014),

$$\frac{M_{\text{HI}}}{L_B} = K \left(\frac{L_B}{L_{B*}} \right)^\beta, \quad (3)$$

where K is a constant equal to M_{HI}/L_B for $L_B = L_{B*}$. Combining the above equations, and integrating over the B-band luminosity function (this time, for all M_B), we obtain

$$\rho_{\text{HI}}/\rho_{c,0} = \frac{K}{\rho_{c,0}} L_{B*} \phi_* \Gamma(\alpha + \beta + 2, L_{\text{min}}/L_{B*}), \quad (4)$$

where L_{min} is the faint-end cut-off of the B-band luminosity function. The result is insensitive to the choice of L_{min}/L_{B*} as long as this value is $\lesssim 10^{-3}$.

There is currently no direct estimate of β at $z \approx 0.3$. We hence assume that the local $M_{\text{HI}} - M_B$ relation ($\beta = -0.15$; Dénes et al. 2014) is valid at $z \approx 0.3$. We then obtain $K = (0.73 \pm 0.11) M_\odot/L_{B\odot}$. We also include the effect

of cosmic variance by using the estimated cosmic variance of 18% in the luminosity density ϕ_* at $z \approx 0.3$ for the EGS (Willmer et al. 2006). Replacing for K in equation (4), with $L_{\min}/L_{B^*} = 10^{-4}$, we obtain $\rho_{\text{HI}} = (6.5 \pm 1.0 \pm 1.2) \times 10^7 M_{\odot} \text{Mpc}^{-3}$ and $\rho_{\text{HI}}/\rho_{c,0} = (4.81 \pm 0.75 \pm 0.87) \times 10^{-4}$, where the second uncertainty in the two expressions stems from cosmic variance. Note that using the $M_{\text{HI}} - M_{\text{B}}$ relation to estimate $\rho_{\text{HI}}/\rho_{c,0}$ in galaxies with $M_{\text{B}} \leq -17$ yields values of $\rho_{\text{HI}}/\rho_{c,0}$ consistent (within the statistical errors) with our estimate above.

In the local Universe, $\rho_{\text{HI}}/\rho_{c,0}$ has long been accurately estimated via blind HI 21 cm emission surveys (e.g. Zwaan et al. 2005; Jones et al. 2018). Conversely, at high redshifts, $z > 2$, the incidence of damped Lyman- α absorbers (DLAs) in QSO spectra from the Sloan Digital Sky Survey has been used to infer $\rho_{\text{HI}}/\rho_{c,0}$ (e.g. Prochaska et al. 2005; Noterdaeme et al. 2012). These studies have shown that $\rho_{\text{HI}}/\rho_{c,0}$ declines by only a factor of ≈ 2 from $z \approx 2.2$ to $z \approx 0$. However, the need for ultraviolet spectroscopy to detect DLAs at $z < 1.7$ and the weakness of the HI 21 cm line has meant that it has been difficult to study the evolution of $\rho_{\text{HI}}/\rho_{c,0}$ at intermediate redshifts, $z \approx 0.2 - 2.2$. Our result, $\rho_{\text{HI}}/\rho_{c,0} = (4.81 \pm 0.75) \times 10^{-4}$, is the first statistically-significant estimate of $\rho_{\text{HI}}/\rho_{c,0}$ at these redshifts.

Fig. 4 shows $\rho_{\text{HI}}/\rho_{c,0}$ versus redshift, from a range of measurements at $z \approx 0 - 5$. It is clear that our estimate of $\rho_{\text{HI}}/\rho_{c,0}$ at $z \approx 0.34$ is consistent with the value in the local

Universe (Jones et al. 2018), indicating no significant evolution in $\rho_{\text{HI}}/\rho_{c,0}$ over $0 < z < 0.4$.

5. SUMMARY

We have used a deep uGMRT 970 – 1370 MHz observation of the EGS to measure the average HI mass and the median total SFR of a sample of 445 blue star-forming galaxies at $z \approx 0.2 - 0.4$, by stacking their HI 21 cm line and 1.4 GHz continuum emission. We obtain $\langle M_{\text{HI}} \rangle = (4.93 \pm 0.70) \times 10^9 M_{\odot}$ and $\text{SFR} = (0.54 \pm 0.06) M_{\odot} \text{yr}^{-1}$, implying an HI depletion timescale of $\langle \Delta t_{\text{HI}} \rangle \approx 9 \text{ Gyr}$. This is comparable to the HI depletion timescale in local star-forming galaxies, but far larger than the same timescale for star-forming galaxies at $z \approx 1.3$. We obtain a gas fraction of $M_{\text{HI}}/M_* \approx 1.2$, larger than typical values in local star-forming galaxies. Finally, we obtain a cosmic HI mass density of $\rho_{\text{HI}}/\rho_{c,0} = (4.81 \pm 0.75) \times 10^{-4}$, consistent with the value of $\rho_{\text{HI}}/\rho_{c,0}$ in the local Universe, and with $\approx 90\%$ arising from bright galaxies, with $M_{\text{B}} \leq -17$.

ACKNOWLEDGEMENTS

We thank the staff of the GMRT who have made these observations possible. The GMRT is run by the National Centre for Radio Astrophysics of the Tata Institute of Fundamental Research. NK acknowledges support from the Department of Science and Technology via a Swarnajayanti Fellowship (DST/SJF/PSA-01/2012-13).

REFERENCES

- Bera, A., Kanekar, N., Weiner, B. J., Sethi, S., & Dwarakanath, K. S. 2018, *ApJ*, 865, 39
- Catinella, B., & Cortese, L. 2015, *MNRAS*, 446, 3526
- Catinella, B., et al. 2018, *MNRAS*, 476, 875
- Chengalur, J. N., Braun, R., & Wieringa, M. 2001, *A&A*, 372, 768
- Coil, A. L., et al. 2008, *ApJ*, 672, 153
- Condon, J. J., Cotton, W. D., & Broderick, J. J. 2002, *AJ*, 124, 675
- Cooper, M. C., et al. 2012, *MNRAS*, 419, 3018
- Crighton, N. H. M., et al. 2015, *MNRAS*, 452, 217
- Decarli, R., et al. 2019, arXiv e-prints, arXiv:1903.09164
- Delhaize, J., Meyer, M. J., Staveley-Smith, L., & Boyle, B. J. 2013, *MNRAS*, 433, 1398
- Dénes, H., Kilborn, V. A., & Koribalski, B. S. 2014, *MNRAS*, 444, 667
- Fernández, X., et al. 2016, *ApJL*, 824, L1
- Hopkins, A. M., & Beacom, J. F. 2006, *ApJ*, 651, 142
- Jaffé, Y. L., Poggianti, B. M., Verheijen, M. A. W., Deshev, B. Z., & van Gorkom, J. H. 2013, *MNRAS*, 431, 2111
- Jones, M. G., Haynes, M. P., Giovanelli, R., & Moorman, C. 2018, *MNRAS*, 477, 2
- Kanekar, N., Sethi, S., & Dwarakanath, K. S. 2016, *ApJL*, 818, L28
- Lah, P., et al. 2007, *MNRAS*, 376, 1357
- Mostek, N., Coil, A. L., Moustakas, J., Salim, S., & Weiner, B. J. 2012, *ApJ*, 746, 124
- Neeleman, M., Prochaska, J. X., Ribaldo, J., Lehner, N., Howk, J. C., Rafelski, M., & Kanekar, N. 2016, *ApJ*, 818, 113
- Newman, J. A., et al. 2013, *ApJS*, 208, 5
- Noeske, K. G., et al. 2007, *ApJL*, 660, L43
- Noterdaeme, P., et al. 2012, *A&A*, 547, L1
- Pavesi, R., et al. 2018, *ApJ*, 864, 49
- Prochaska, J. X., Herbert-Fort, S., & Wolfe, A. M. 2005, *ApJ*, 635, 123
- Rao, S. M., et al. 2017, *MNRAS*, 471, 3428
- Rhee, J., Lah, P., Briggs, F. H., Chengalur, J. N., Colless, M., Willner, S. P., Ashby, M. L. N., & Le Fèvre, O. 2018, *MNRAS*, 473, 1879
- Rhee, J., Zwaan, M. A., Briggs, F. H., Chengalur, J. N., Lah, P., Oosterloo, T., & van der Hulst, T. 2013, *MNRAS*, 435, 2693
- Saintonge, A., et al. 2017, *ApJS*, 233, 22
- Schiminovich, D., et al. 2010, *MNRAS*, 408, 919

- Stefanon, M., et al. 2017, ApJS, 229, 32
- Tacconi, L. J., et al. 2018, ApJ, 853, 179
- Wang, J., Koribalski, B. S., Serra, P., van der Hulst, T., Roychowdhury, S., Kamphuis, P., & Chengalur, J. N. 2016, MNRAS, 460, 2143
- Willmer, C. N. A., et al. 2006, ApJ, 647, 853
- Wong, O. I., Meurer, G. R., Zheng, Z., Heckman, T. M., Thilker, D. A., & Zwaan, M. A. 2016, MNRAS, 460, 1106
- Yun, M. S., Reddy, N. A., & Condon, J. J. 2001, ApJ, 554, 803
- Zwaan, M. A., Meyer, M. J., Staveley-Smith, L., & Webster, R. L. 2005, MNRAS, 359, L30